

**Assessing Snow Albedo Feedback in
Simulated Climate Change**

Xin Qu and Alex Hall

Department of Atmospheric and Oceanic Sciences

University of California, Los Angeles

Los Angeles, California

corresponding author address:

Xin Qu

Department of Atmospheric and Oceanic Sciences

University of California, Los Angeles

Los Angeles, CA 90095

e-mail: xinqu@atmos.ucla.edu

For JCLI CCSM Special Issue

Abstract

We isolate and quantify the two factors controlling Northern Hemisphere springtime snow albedo feedback in transient climate change based on scenario runs of 17 climate models used in the IPCC 4th Assessment. The first factor is the dependence of planetary albedo on surface albedo, representing the atmosphere's attenuation effect on surface albedo anomalies. It is potentially a major source of divergence in simulations of snow albedo feedback because of large differences in simulated cloud fields in Northern Hemisphere land areas. To calculate it, we develop an analytical model governing planetary albedo. We show detailed validation of the analytical model for two of the simulations, CCSM3.0 and CM2.0, demonstrating that it facilitates highly accurate calculation of the dependence of planetary albedo on surface albedo given readily-available simulation output. We find in all simulations surface albedo anomalies are attenuated by approximately half in Northern Hemisphere land areas as they are transformed into planetary albedo anomalies. The intermodel standard deviation in this factor is surprisingly small, less than 10% of the mean. Moreover, when we calculate an observational estimate of this factor by applying the same method to the satellite-based ISCCP data, we find most simulations agree with ISCCP values to within about 10%, in spite of further disagreements between observed and simulated cloud fields. This suggests even large relative errors in simulated cloud fields do not result in significant error in this factor, enhancing confidence in climate models. The second factor, related exclusively to surface processes, is the change in surface albedo associated with an anthropogenically-induced temperature change in Northern Hemisphere land areas. It exhibits much more intermodel variability. Its standard deviation is about 1/3 of the mean, with the largest value being approximately three times larger than the smallest. Therefore this factor is unquestionably the main source of the large

divergence in simulations of snow albedo feedback. To reduce the divergence, attention should be focused on differing parameterizations of snow processes, rather than intermodel variations in the attenuation effect of the atmosphere on surface albedo anomalies.

1. Introduction

As surface air temperature increases in climate change simulations with coupled land-ocean-atmosphere models, snow over the northern hemisphere (NH) extratropics retreats, revealing land surface that is much less reflective of solar radiation. The additional absorbed solar radiation results in more warming (Cubasch et al. 2001; Holland and Bitz 2003). This positive feedback, the so-called snow albedo feedback, accounts for about half of the additional net incoming solar radiation associated with the NH cryosphere retreat in equilibrium climate change simulations (Hall 2004). The satellite record also supports the idea of a positive snow albedo feedback. By correlating ERBE top-of-the-atmosphere short-wave fluxes and satellite-observed snow extent in the NH extratropics, Groisman et al. (1994a, b) pointed out that a large portion of the NH warming for the last two decades of the 20th century can be attributed to snow albedo changes. Despite the consensus on the sign of the feedback, its strength as seen in climate change simulations carried out over the past two decades varies significantly (Cess et al. 1991; Randall et al. 1994; Cubasch et al. 2001; Holland and Bitz 2003). These differences become a source of divergence in simulated climate change (Cubasch et al. 2001; Holland and Bitz 2003).

According to the classic climate sensitivity framework (e.g., Cess and Potter 1988), the strength of snow albedo feedback in climate change can be quantified by the variation in net incoming shortwave radiation (Q) with surface air temperature (T_s) due to changes in surface albedo (α_s):

$$\left(\frac{\partial Q}{\partial T_s}\right)_{SAF} = \frac{\partial Q}{\partial \alpha_s} \cdot \frac{\Delta \alpha_s}{\Delta T_s} \quad (1)$$

where the subscript SAF is used to emphasize that the partial derivative refers only to changes in solar radiation with surface temperature that occur due to changes in the snow pack, rather than changes in cloudiness or other factors that could affect solar radiation. According to eq. (1), snow albedo feedback is the product of two terms, one representing the dependence of net incoming solar radiation on surface albedo ($\partial Q/\partial\alpha_s$), and another representing the change in surface albedo induced by a unit temperature change ($\Delta\alpha_s/\Delta T_s$).

The partial derivative, $\partial Q/\partial\alpha_s$ (first term in eq. (1)) can be rewritten as follows:

$$\frac{\partial Q}{\partial\alpha_s} = -I_t \cdot \frac{\partial\alpha_p}{\partial\alpha_s} \quad (2)$$

where I_t is the incoming solar radiation at the top of atmosphere (TOA), which we take to be a constant, and $\partial\alpha_p/\partial\alpha_s$ is the variation in planetary albedo with snow albedo, with other factors such as water vapor concentration and cloud fixed. It represents the attenuation effect of the atmosphere on snow albedo anomalies, which results from two processes: First, incoming solar photons at the TOA are partly absorbed and reflected back to space by the atmosphere, reducing the number reaching the surface; Second, solar photons initially reflected by the surface are partly absorbed and reflected back to the surface by the atmosphere, reducing the number reaching the TOA. Obviously the more the atmosphere absorbs and scatters solar radiation due to factors such as water vapor concentration and cloudiness, the greater the atmospheric attenuation of snow albedo anomalies. Because mean water vapor concentration and cloudiness differ among climate models, values of $\partial\alpha_p/\partial\alpha_s$ may vary from model to model, creating divergence in

the strength of simulated snow albedo feedback quite apart from divergence which arises from differing simulations of surface processes, represented by the second term in eq. (1), $\Delta\alpha_s/\Delta T_s$. We wish to isolate and assess this. Cloud changes associated with cloud feedback processes also result in changes in the attenuation effect of the atmosphere on snow albedo anomalies, and in turn may cause $\partial\alpha_p/\partial\alpha_s$ to vary significantly with time as the overall climate changes. This may make it difficult to use a single value to represent the strength of this aspect of snow albedo feedback. We wish to determine whether or not this effect is important.

We also aim to isolate and assess the divergence resulting from the second term of eq. (1), $\Delta\alpha_s/\Delta T_s$. However, this term is straightforward to quantify from model output by simply dividing the simulated change in α_s by the change in T_s . The first term, on the other hand, is difficult to calculate directly from model output because it is a partial derivative assuming fixed clouds and water vapor. Previous efforts have focused on the ratio, $\Delta\alpha_p/\Delta\alpha_s$, rather than $\partial\alpha_p/\partial\alpha_s$ (Cess 1991 et al. 1991; Randall et al. 1994), where $\Delta\alpha_s$ and $\Delta\alpha_p$ represent simulated changes in surface and planetary albedo from the current climate to the future warmer climate, calculated from TOA and surface fluxes commonly stored by climate simulations. However, this approach conflates model divergence stemming from cloud feedback with that stemming from snow albedo feedback, since cloud changes contaminate TOA solar fluxes used to calculate planetary albedo.

Because of this difficulty, the focus of much of this paper is isolating the $\partial\alpha_p/\partial\alpha_s$ component of snow albedo feedback, done by developing an analytical model of planetary albedo. In the analytical model, planetary albedo is represented as a function

of known model variables, such as surface albedo, cloud cover and cloud optical thickness. We determine the coefficients of the terms relating these variables to planetary albedo empirically from model output. With the analytical model, calculation of a true partial derivative with respect to surface albedo is straightforward. Of course, our results rest upon the ability of the analytical model to capture simulated variations in planetary albedo. We therefore validate it in transient climate change simulations with several new versions of state-of-the-art models of the Fourth Assessment (AR4) of the Intergovernmental Panel on Climate Change (IPCC) and find that it does remarkably well. This allows us to use the analytical model to calculate values of $\partial\alpha_p/\partial\alpha_s$ in these models with a high degree of accuracy. Moreover, we find we can apply the analytical model with the same high degree of accuracy to the International Satellite Cloud Climatology Project (ISCCP) data from 1984 to 2000. This facilitates the use of satellite data to assess the realism of the simulations. Though we validate the analytical model in all the simulations, for simplicity we show details only for two of the models, the National Center for Atmospheric Research (NCAR) CCSM3.0 and the Geophysical Fluid Dynamics Laboratory (GFDL) CM2.0. Our study focuses on springtime (MAM). The reason for this is that over half the increase in net incoming solar radiation associated with snow retreat occurs during this season in climate change simulations (Hall 2004), as both snow extent and incoming solar radiation are relatively large. However, the methods we develop here can be easily extended to other seasons.

Our results are presented as follows: A brief description of climate models and ISCCP data sets is given in Section 2, followed in Section 3 by an illustration of how both surface albedo and clouds contribute to the planetary albedo change from the current

to the future climate in the NH extratropics using the CM2.0 and CCSM3.0 simulations as examples. An analytical model for planetary albedo is developed and validated against simulated and ISCCP data sets in Section 4. In Section 5, we use this model to obtain an expression for $\partial\alpha_p/\partial\alpha_s$ and assess it in the current and future climate based on simulated and ISCCP data sets. Summary and implications are found in Section 6, where we also present calculations of the $\Delta\alpha_s/\Delta T_s$ term of eq. (1) for the AR4 models. In this section we compare the intermodel divergence in this term to the divergence in the $\partial\alpha_p/\partial\alpha_s$ term to see which accounts for the most overall intermodel divergence in simulations of snow albedo feedback.

2. Models and observations

2.1 Models

We use output from the 20th and 22nd centuries of transient climate change experiments with 17 AR4 models (see Table 1). The 20th century climate is simulated in these models by imposing estimates of climate forcings from the period 1901-2000, while the 22nd century is simulated by imposing the A1B emissions scenario (Prentice et al. 2001).

Since the analytical model is validated in detail only for NCAR CCSM3.0 and GFDL CM2.0 models, only these two models are briefly described here. NCAR CCSM3.0 (referred to hereafter as CCSM3.0) consists of general circulation models of the atmosphere and ocean, a land surface model and a sea-ice model. The atmospheric component (Collins et al. 2004) has horizontal resolution of approximately 1.4° latitude by 1.4° longitude and 26 vertical finite difference levels. The land surface component contains

a simplified treatment of surface processes responsible for land-atmosphere exchange of heat, water and momentum (Oleson et al. 2004). A canopy radiative transfer scheme is used to calculate surface albedo, accounting for the joint albedo effect of canopy and ground. Ground albedo is a weighted combination of soil and snow albedos by snow cover, which in turn is a function of snow depth. Snow albedo is parameterized as a function of solar zenith angle and snow age. The oceanic component (Smith and Gent 2004) has 320×384 points horizontally and 40 ocean levels vertically. The sea-ice component includes a subgrid-scale ice thickness distribution, energy conserving thermodynamics, and elastic-viscous-plastic dynamics (Briegleb et al. 2004).

Similar to CCSM3.0, the GFDL CM2.0 (referred to hereafter as CM2.0) consists of general circulation models of the atmosphere and ocean, a land surface model and a sea ice model. The atmosphere component uses a new grid point dynamical core, a prognostic cloud scheme and a multi-species aerosol climatology (GAMDT 2005). It has horizontal resolution of 2.5° longitude by 2° latitude and 24 vertical levels. The land component is based on the Land Dynamics model described by Milly and Shmakin (2002). Surface albedo over snow-covered regions is parameterized as an average of snow-free surface albedo and snow albedo, which are weighted by snow cover. Snow cover is in turn a function of snow depth. Snow albedo is parameterized as a function of surface temperature. This scheme does not explicitly include canopy effects in its calculation of surface albedo, as is the case with CCSM3.0. The model has a full 3-dimensional dynamical ocean as well as a complex sea ice model; however, no official documentation of the ocean and sea ice components of CM2.0 was available when this article was composed.

2.2 ISCCP data sets

The ISCCP D-series cloud data sets used in this study are based on observations from a suite of operational weather satellites measuring the temporal and spatial distribution of visible (VIS wavelength $\approx 0.6 \mu m$), near-infrared (NIR wavelength $\approx 3.7 \mu m$) and infrared (IR wavelength $\approx 11 \mu m$) radiation. These measurements are then employed to retrieve information about clouds, such as cloud cover, cloud optical thickness and cloud top pressure (Rossow and Schiffer 1991; Rossow and Garder 1993a,b; Rossow et al. 1993; Rossow and Schiffer 1999). Three changes have been made in the D-series datasets to enhance the accuracy of cloud detection over snow- and ice-covered surfaces (Rossow and Schiffer 1999): (1) most importantly, a new threshold test on $3.7 \mu m$ radiances was used, exploiting significantly greater contrast between cloudy and clear scenes over snow- and ice-covered surfaces at this frequency than at $0.6 \mu m$; (2) at the high latitudes, the visible radiance threshold test was changed to a visible reflectance threshold test; (3) over snow and ice in the polar regions, both the VIS and IR thresholds were lowered. Together these improvements have been shown to increase significantly low-level cloud detection sensitivity over snow and ice and reduce the biases in cloud optical thickness of previous ISCCP C-series datasets in these regions.

Accompanying the ISCCP D-series cloud data sets are radiative flux data sets containing solar and infrared radiative fluxes at the TOA and surface for both clear-sky and full-sky situations. They are calculated by specifying the following information in a radiative transfer model (Zhang et al. 2004): (1) atmospheric temperature and humidity profiles; (2) vertical profiles of various atmospheric gases, such as CO_2 , O_3 , O_2

and CH₄; (3) vertical aerosol profiles for the troposphere and stratosphere; (4) ISCCP D-series cloud datasets; (5) snow and ice cover data. All the data mentioned above are time-varying so that observed variations in radiative properties of the atmosphere and surface are reflected in the fluxes at the TOA and surface.

These data sets are provided on a global $2.5^0 \times 2.5^0$ grid and cover the period from 1984 to 2000.

3. Simulated reduction in planetary albedo over NH extratropical land areas

In this section, we demonstrate how both surface albedo and clouds contribute to the planetary albedo change from the current to the future climate in NH extratropical land areas using the CM2.0 and CCSM3.0 simulations as examples.

Fig 1 shows simulated changes in springtime surface albedo (α_s), cloud cover (c), logarithm of cloud optical thickness ($\ln(\tau + 1)$) and planetary albedo (α_p) from the 20th to the 22nd century climate in the NH extratropics. We show the logarithm of cloud optical thickness (τ) rather than τ itself to take account of the quasi-logarithmic dependence of cloud albedo on τ (Rossow et al. 1996). Because cloud liquid water path (c_{lwp}) and ice water path (c_{iwp}) rather than τ are provided by the CM2.0 and CCSM3.0 data sets, a relation is used to convert c_{lwp} and c_{iwp} into τ :

$$\tau = \kappa_1 \cdot c_{lwp} + \kappa_2 \cdot c_{iwp} \quad (3)$$

where κ_1 and κ_2 are assumed to be 0.16 and 0.10, respectively, in accordance with

the values used by the ISCCP (Rossow et al. 1996). This facilitates the comparison between ISCCP data sets and model data sets in the current climate in Sections 4 and 5.

As shown in Fig 1, surface albedo decreases in the warmer climate in both CM2.0 and CCSM3.0 throughout the NH extratropical land areas, especially northern Canada, western Russia and Tibetan plateau. However, the decrease is much greater in CM2.0 than CCSM3.0. The surface albedo reductions averaged over extratropical North America and Eurasia in CM2.0 are about 5-8%, but are only about 3-4% in CCSM3.0 (see Fig 2). The surface albedo reduction in CCSM3.0 is smaller because surface albedo is less sensitive to the change in surface air temperature and also because the overall warming is smaller in the model. As shown in Table 2, the ratio, $\Delta\alpha_s/\Delta T_s$ in CCSM3.0 is about 10% and 50% smaller than that of CM2.0 in extratropical Eurasia and North America.

Changes in cloud cover and cloud optical thickness simulated in CM2.0 and CCSM3.0 differ not only in amplitude, but also in sign. Cloud cover in CM2.0 decreases in the warmer climate nearly everywhere in North America and Eurasia, especially in the western United States and western Europe. This reduction averaged over extratropical North America and Eurasia is about 1% and 4% (see Fig 2). In contrast, cloud cover simulated in CCSM3.0 increases in the high latitudes of Eurasia and nearly everywhere in North America, especially in northern Canada, and decreases only in the middle latitudes of Eurasia. Cloud cover averaged over extratropical North America increases 2%, but decreases 1% over extratropical Eurasia (see Fig 2). The logarithm of cloud optical thickness in CM2.0 increases in the warmer climate nearly everywhere

in North America and Eurasia. This increase averaged over extratropical North America and Eurasia is about 0.2-0.3 (see Fig 2), about one tenth of the mean springtime value (2.3). The logarithm of cloud optical thickness in CCSM3.0 increases in the high latitudes of both Eurasia and North America, but decreases in the middle latitudes. This change averaged over extratropical North America is 0.1, and is slightly positive over extratropical Eurasia (Fig 2). The disparity in changes in cloud fields between the two models shown in Figs 1 and 2 is also seen among other AR4 models (not shown). This is consistent with the wide divergence in simulations of cloud feedback among current climate models. We are particularly concerned with this divergence because it complicates our ability to assess snow albedo feedback independently of cloud changes.

Planetary albedo in CM2.0 and CCSM3.0 decreases everywhere in extratropical North America and Eurasia, especially in regions with strong surface albedo reduction, such as northern Canada, western Russia and Tibetan plateau. This demonstrates the effect of snow retreat on the top-of-the-atmosphere short-wave fluxes. However, the effect of cloud variations is visible in regions with small snow albedo reduction, such as western Europe. As shown in Fig 2, the planetary albedo reduction averaged over extratropical North America and Eurasia in CM2.0 is about 3%, about half the albedo reduction at the surface. The planetary albedo reduction averaged over extratropical Eurasia in CCSM3.0 is about 1.6%, also about half the albedo signature at the surface. The planetary albedo reduction averaged over extratropical North America in CCSM3.0 is only about 1%, considerably less than that averaged over extratropical Eurasia, in spite of the fact that the surface albedo reduction over North America is slightly greater than that over Eurasia. It seems likely that the substantial increases in cloud cover and

cloud optical thickness over North America are responsible for this disproportionately small reduction in planetary albedo, highlighting the need for a method to quantify the dependence of planetary albedo on surface albedo independently of cloud variations.

4. An analytical model to understand planetary albedo

In the previous section, we showed that surface albedo, cloud cover and cloud optical thickness probably all contribute to the simulated planetary albedo change in the warmer climate in two AR4 transient climate change simulations. To isolate the surface contribution, we develop an analytical model governing planetary albedo, and validate it against simulated and satellite-based data sets. This model relates full-sky planetary albedo to known quantities, including clear-sky planetary albedo, cloud cover, cloud optical thickness and surface albedo. This allows us to generate an analytical expression for $\partial\alpha_p/\partial\alpha_s$. We can then compare this quantity among models and satellite-based data sets.

This model is derived as follows: Full-sky planetary albedo can be written as the weighted mean of clear-sky planetary albedo (α_p^{cr}) and cloudy-sky planetary albedo (α_p^{cd}):

$$\alpha_p = (1 - c) \cdot \alpha_p^{cr} + c \cdot \alpha_p^{cd} \quad (4)$$

In eq. (4), α_p^{cr} is given as follows:

$$\alpha_p^{cr} = \alpha_a^{cr} + T_a^{cr} \cdot \alpha_s \quad (5)$$

which is the sum of clear-sky atmospheric albedo to incoming solar radiation (α_a^{cr}),

and a surface albedo component, which is the product of α_s and an effective clear-sky atmospheric transmissivity, T_a^{cr} . In eq. (4), α_p^{cd} is given as follows:

$$\alpha_p^{cd} = \alpha_a^{cd} + T_a^{cd} \cdot \alpha_s \quad (6)$$

which is the sum of cloudy sky atmospheric albedo to incoming solar radiation (α_a^{cd}), and a surface albedo component, which is the product of α_s and an effective cloudy sky atmospheric transmissivity, T_a^{cd} . We model the difference between clear and cloudy sky atmospheric albedo as proportional to the logarithm of cloud optical thickness, thereby linking α_a^{cr} in eq. (5) and α_a^{cd} in eq. (6):

$$\alpha_a^{cd} = \alpha_a^{cr} + \varepsilon_1 \cdot \ln(\tau + 1) \quad (7)$$

In eq. (7), ε_1 is the linear coefficient relating the logarithm of cloud optical thickness to the cloudy-sky atmospheric albedo. Similarly, we model the difference between clear and cloudy sky effective transmissivity as proportional to the logarithm of cloud optical thickness, thereby linking T_a^{cr} in eq. (5) and T_a^{cd} in eq. (6):

$$T_a^{cd} = T_a^{cr} - \varepsilon_2 \cdot \ln(\tau + 1) \quad (8)$$

where ε_2 is the linear coefficient relating the logarithm of cloud optical thickness to the effective cloudy-sky atmospheric transmissivity.

We plug eqs. (5)-(8) into (4), and rearrange it into

$$\alpha_p = \alpha_p^{cr} + c \cdot \ln(\tau + 1) \cdot (\varepsilon_1 - \varepsilon_2 \cdot \alpha_s) \quad (9)$$

We can rewrite eq. (9) as follows:

$$\alpha_p - \alpha_p^{cr} = \varepsilon_1 \cdot c \cdot \ln(\tau + 1) - \varepsilon_2 \cdot c \cdot \ln(\tau + 1) \cdot \alpha_s \quad (10)$$

Because α_p , α_p^{cr} , c , $\ln(\tau + 1)$ and α_s are given in models and observations, values of the two linear coefficients, ε_1 and ε_2 , can be readily obtained by regressing $(\alpha_p - \alpha_p^{cr})$ onto $c \cdot \ln(\tau + 1)$ and $c \cdot \ln(\tau + 1) \cdot \alpha_s$.

Eq. (9) is our analytical model for planetary albedo. To test how well it captures planetary albedo and its temporal and spatial variability, we apply it to ISCCP and the AR4 simulations of the current climate. First, α_p , α_p^{cr} , c , $\ln(\tau + 1)$ and α_s in March, April and May were averaged to get a yearly time-series of springtime-mean values at each location within extratropical North America and Eurasia. The time period used was the 20th century in the case of the AR4 simulations and the years 1984-2000 for the ISCCP data set. Then, the difference between full-sky and clear-sky planetary albedo, $(\alpha_p - \alpha_p^{cr})$ was regressed onto $c \cdot \ln(\tau + 1)$ and $c \cdot \ln(\tau + 1) \cdot \alpha_s$ to obtain values of ε_1 and ε_2 . We perform the regression calculation based on concatenated time series of all locations within extratropical North America and Eurasia, so that we are attempting to capture both interannual and geographical variability in planetary albedo. This provides samples large enough to achieve stable statistics in both satellite data sets and

simulations, the size of samples being larger than 8000. We can then model interannual and geographical variations in planetary albedo by plugging in these values of ε_1 and ε_2 , as well as values of c , τ , α_p^{cr} and α_s into eq. (9). As a example, Fig 3 shows the scatterplot of modeled planetary albedo against actual planetary albedo in ISCCP data sets and two simulations: CM2.0 and CCSM3.0. They almost exactly follow a diagonal line, and the correlation coefficient shown in the right-bottom corner of each panel is very close to unity, implying nearly perfect agreement. Eq. (9) is also used to model planetary albedo in the climate of the 22nd century in CM2.0 and CCSM3.0 by plugging in the values of ε_1 and ε_2 obtained from the current climate, as well as values of c , τ , α_p^{cr} and α_s in the future climate. Similarly, modeled and simulated planetary albedo in the two models are nearly perfectly correlated (not shown). Eq. (9) captures the physical relationship seen in the models and ISCCP data set among planetary albedo, surface albedo and clouds extremely well not only in the CCSM3.0 and CM2.0 simulations, but also the other AR4 models. Plots for the other AR4 models similar to Fig. 3 (not shown) are almost identical, with a nearly one-to-one correspondence between modeled and simulated planetary albedo.

To reveal physical insights behind eq. (9), we rearrange it:

$$\alpha_p = (\alpha_a^{cr} + \varepsilon_1 \cdot c \cdot \ln(\tau + 1)) + (T_a^{cr} - \varepsilon_2 \cdot c \cdot \ln(\tau + 1)) \cdot \alpha_s \quad (11)$$

The first term, $(\alpha_a^{cr} + \varepsilon_1 \cdot c \cdot \ln(\tau + 1))$ in eq. (11) can be viewed as an effective full-sky atmospheric albedo. It is attributed partly to the clear-sky atmosphere (α_a^{cr}) and partly to clouds ($\varepsilon_1 \cdot c \cdot \ln(\tau + 1)$). The second term, $(T_a^{cr} - \varepsilon_2 \cdot c \cdot \ln(\tau + 1)) \cdot \alpha_s$ can be viewed as

a surface albedo component of full-sky planetary albedo, which is the product of α_s and an effective full-sky atmospheric transmissivity ($T_a^{cr} - \varepsilon_2 \cdot c \cdot \ln(\tau + 1)$). The latter is attributed partly to the clear-sky atmosphere (T_a^{cr}) and partly to clouds ($-\varepsilon_2 \cdot c \cdot \ln(\tau + 1)$). The two terms involving clouds in eq. (11), $(\varepsilon_1 \cdot c \cdot \ln(\tau + 1))$ and $(-\varepsilon_2 \cdot c \cdot \ln(\tau + 1) \cdot \alpha_s)$ represent two effects on planetary albedo: (1) clouds increase planetary albedo through their own reflectivity; (2) clouds decrease the surface contribution to planetary albedo by reducing the effective full-sky atmospheric transmissivity. In both cases, the effect is proportional to the product of cloud cover and the logarithm of cloud optical thickness.

5. Dependence of planetary albedo on surface albedo ($\partial\alpha_p/\partial\alpha_s$)

Eq. (11) is such a successful model for planetary albedo that we can use it to derive an accurate expression for the first term of eq. (1), the partial derivative, $\partial\alpha_p/\partial\alpha_s$:

$$\partial\alpha_p/\partial\alpha_s = T_a^{cr} - \varepsilon_2 \cdot c \cdot \ln(\tau + 1) \quad (12)$$

The right-hand side of eq. (12) represents the total attenuation effect of the atmosphere on the surface's contribution to planetary albedo fluctuation. This includes a contribution from the cloudless atmosphere, represented by T_a^{cr} , as well as a contribution from cloud, being proportional to the product of cloud cover and the logarithm of cloud optical thickness. The direct effects of the changes in cloudiness on planetary albedo are not included in eq. (12), and so are not conflated with the effects of changes in surface albedo, as is the case if the dependence of planetary albedo on surface albedo is measured by simply regressing planetary albedo variations onto their counterparts at

the surface. This points to the relevance of our analytical model in unraveling surface and cloud's contributions to planetary albedo variations in cryosphere regions. We will use eq. (12) to assess the values of $\partial\alpha_p/\partial\alpha_s$ in the current climate and future climate.

The quantities c and τ are given by the ISCCP and model data sets, while ε_2 is known from regression analysis relying on eq. (10). The unknown quantity on the right-hand side of eq. (12) is therefore the clear-sky effective atmospheric transmissivity, T_a^{cr} . Relying on eq. (5), we can obtain it by regressing clear-sky planetary albedo, α_p^{cr} onto surface albedo, α_s . In analogy with Fig 3, we show a scatterplot of modeled clear-sky planetary albedo against the actual clear-sky planetary albedo in ISCCP, CM2.0 and CCSM3.0 data sets in Fig 4 as a validation of this regression model. They follow a diagonal line almost exactly and the correlation coefficient, shown in the right-bottom corner of each scatterplot, is very close to unity, implying nearly perfect agreement. Fig 5 shows values of T_a^{cr} seen in ISCCP, CM2.0 and CCSM3.0 in North America and Eurasia. Values of T_a^{cr} in the current climate are comparable among ISCCP, CM2.0 and CCSM3.0, and in the future climate between CM2.0 and CCSM3.0 in both continents, being about 0.7. This is also true for other simulations (not shown). The clear-sky atmosphere attenuates surface albedo fluctuations so that their magnitudes are consistently reduced by about 30% as they are mirrored in planetary albedo variations.

According to Fig 5, there is also a reasonable agreement in values of $\varepsilon_2 \cdot c \cdot \ln(\tau + 1)$ in the current and future climate in both continents, all being about 1/3 as large as values of T_a^{cr} . Values of $\varepsilon_2 \cdot c \cdot \ln(\tau + 1)$ are relatively small because clouds over the extratropics are generally not very thick (mean values of $\ln(\tau + 1)$ is about 2.3) compared to deeper clouds in the tropics (mean values of $\ln(\tau + 1)$ is about 4) and also because a substantial

fraction of the sky is clear in NH snow-covered regions (mean cloud cover is about 60-70%). Because values of ε_2 , the regression coefficient relating cloud optical thickness to cloudy sky transmissivity are generally smaller than 0.16 (see Table 3), differences in values of $\varepsilon_2 \cdot c \cdot \ln(\tau + 1)$ in the current and future climate among the three data sets are generally smaller than 0.1 (see Table 3), in spite of the fact that cloud fields differ somehow in the current and future climate among the three data sets (Table 3).

The mean values of $\partial\alpha_p/\partial\alpha_s$ seen in ISCCP, CM2.0 and CCSM3.0 in the current and future climate have general agreement, all being about 0.5 (Fig 5), implying the size of surface-induced planetary albedo fluctuations in the NH extratropics is about half the albedo signature at the surface. This is the case in spite of the disparities in cloud fields among ISCCP, CM2.0 and CCSM3, between North America and Eurasia within individual data sets, and within regions going from the present-day to future simulated climates. This demonstrates that disparities in the cloud fields seen in the ISCCP, CM2.0 and CCSM3.0 are not large enough to generate appreciable divergence in values of $\partial\alpha_p/\partial\alpha_s$ in the NH extratropics.

Based on eq. (12), values of $\partial\alpha_p/\partial\alpha_s$ in the other AR4 simulations are calculated and shown in Fig 6. The corresponding values in CM2.0 and CCSM3.0 are also shown in this figure for comparison. Consistent with the agreement between CM2.0 and CCSM3.0, values of $\partial\alpha_p/\partial\alpha_s$ are comparable among all the simulations. The standard deviation of this quantity among all the simulations is 0.04, only about 8% of the mean value (0.52) in both North America and Eurasia. Moreover, in the majority of the simulations, values of $\partial\alpha_p/\partial\alpha_s$ agree with the ISCCP values (represented by the solid lines in Fig 6) to within 10%. This indicates that the $\partial\alpha_p/\partial\alpha_s$ component

of snow albedo feedback simulated in climate models agrees quite well with observations.

6. Summary and Implications

The strength of snow albedo feedback can be quantified as the product of two terms, one representing the dependence of planetary albedo on surface albedo ($\partial\alpha_p/\partial\alpha_s$), and another representing the change in surface albedo induced by a unit temperature change ($\Delta\alpha_s/\Delta T_s$). The $\partial\alpha_p/\partial\alpha_s$ term is the variation in planetary albedo with surface albedo in NH extratropical land areas, with other factors such as water vapor concentration and cloud fixed. However, cloud properties can change substantially over the course of transient climate change experiments, and these can in turn have a large effect on incoming solar radiation. This makes it particularly difficult to quantify the strength of this aspect of snow albedo feedback.

To isolate the surface contribution from that of cloud, we develop an analytical model governing planetary albedo. This model relates full-sky planetary albedo to known quantities, including clear-sky planetary albedo, cloud cover, cloud optical thickness and surface albedo. It captures both interannual and geographical variability in planetary albedo in simulated and satellite-based data sets extremely well. The advantage of this model is that we can use it to derive an expression for a true partial derivative of planetary albedo with respect to surface albedo. It includes a contribution from the cloudless atmosphere, represented by an effective clear-sky atmospheric transmissivity as well as a contribution from cloud, being proportional to the product of cloud cover and logarithm of cloud optical thickness.

There is good agreement in values of the clear-sky component of the atmosphere's

attenuation of surface albedo anomalies, both in the current climate and in the future climate in both North America and Eurasia, all being about 0.7. Values of the cloud contribution to the variation in planetary albedo with surface albedo are about 1/3 the size of clear sky component. Cloud is not the most significant factor controlling the variation in planetary albedo with surface albedo both because clouds over the extratropics is generally not very thick, and because a substantial fraction of the sky is clear in NH snow-covered regions. Therefore differences or errors in mean cloud fields of the magnitude seen in the current generation of climate models are not large enough to cause appreciable divergence or errors in estimates of the variation of planetary albedo with surface albedo in the current climate. For example, differences in values of the cloud contribution to the atmospheric attenuation effect among the three data sets in the current climate are generally only about 10% of the total attenuation effect. Nor are changes in mean cloud fields as a result of climate change large enough to cause the variation of planetary albedo with surface albedo to exhibit significant time dependence. Because of this relative insensitivity to variations in mean cloud fields, the mean values of the variation of planetary albedo with surface albedo seen in the simulated current and future climate are in general agreement, all being about 0.5. This value is also in agreement with the satellite-based ISCCP data set. Therefore we can say with a high degree of confidence that both in simulations and satellite-based data sets, snow-induced planetary albedo anomalies are about half the albedo signature at the surface.

Finally, armed with these conclusions about the $\partial\alpha_p/\partial\alpha_s$ term in eq. (1), we focus on the second term in this equation: $\Delta\alpha_s/\Delta T_s$. This term is related to surface processes

and represents the sensitivity of surface albedo to surface air temperature in the NH extratropics. It is easily quantified in AR4 climate simulations, and we show the results in Fig 7. This quantity varies a great deal from model to model. The standard deviation of this quantity among all the simulations is about 1/3 of the mean value in both North America and Eurasia, much greater than the relative variation in $\partial\alpha_p/\partial\alpha_s$ shown in Fig. 6. And over both North American and Eurasia, the largest value is approximately three times as large as the smallest. Therefore we determine that this term is unquestionably the main source of the large divergence in simulations of snow albedo feedback. To reduce this divergence, attention should be focused on differing parameterizations of surface processes rather than intermodel variations in the attenuation effect of the atmosphere on surface albedo anomalies.

Acknowledgments. This study is based on model integrations performed by NCAR and CRIEPI with support and facilities provided by NSF, DOE, ESC/JAMSTEC and MEXT. The authors acknowledge the international modeling groups for providing their data for analysis, the Program for Climate Model Diagnosis and Intercomparison (PCMDI) for collecting and archiving the model data, the JSC/CLIVAR Working Group on Coupled Modelling (WGCM) and their Coupled Model Intercomparison Project (CMIP) and Climate Simulation Panel for organizing the model data analysis activity, and the IPCC WG1 TSU for technical support. The IPCC Data Archive at Lawrence Livermore National Laboratory is supported by the Office of Science, U.S. Department of Energy. This study was supported by NSF Grant ATM-0135136. But, any opinions, findings, and conclusions or recommendations expressed in this material

are those of the authors and do not necessarily reflect the views of the National Science Foundation. The authors wish to thank Y.-C. Zhang for his help with the ISCCP cloud and flux datasets and two anonymous reviewers for their constructive criticism of this manuscript.

References

- Briegleb, B. P. and coauthors, 2004: Scientific Description of the Sea Ice Component in the Community Climate System Model, Version Three. NCAR/TN-463+STR, NCAR TECHNICAL NOTE.
- Cess, R. D. and coauthors, 1991: Interpretation of snow-climate feedback as produced by 17 general circulation models. *Science*, **253**, 888–892.
- Cess, R. D. and G. L. Potter, 1988: A methodology for understanding and intercomparing atmospheric climate feedback processes in general circulation models. *J. Geophys. Res.*, **93**(D7), 8305–8314.
- Collins, W. D. and coauthors, 2004: Description of the NCAR Community Atmosphere Model (CAM3.0). NCAR/TN-464+STR, NCAR TECHNICAL NOTE.
- Cubasch, U. and coauthors, 2001: Projections of future climate change. *Climate Change 2001: The Scientific Basis*. J. W. Kim and J. Stone, Eds., Cambridge University Press, 525–582.
- GAMDT, 2005: The new GFDL global atmosphere and land model AM2/CM2.0: Evaluation with prescribed SST simulations. Submitted to *J. Climate*.
- Groisman, P. Y., T. R. Karl and R. W. Knight, 1994a: Observed impact of snow cover on the heat balance and the rise of continental spring temperatures. *Science*, **263**, 198–200.
- Groisman, P. Y., T. R. Karl and R. W. Knight, 1994b: Changes of snow cover, tem-

- peratures, and radiative heat balance over the northern hemisphere. *J. Climate*, **7**, 1633–1656.
- Hall, A., 2004: The role of surface albedo feedback in climate. *J. Climate*, **17**, 1550–1568.
- Holland, M. M. and C. M. Bitz, 2003: Polar amplification of climate change in coupled models. *Climate Dyn.*, **21**, 221–232.
- Milly, P. C. D. and A. B. Shmakin, 2002: Global modeling of land water and energy balances. Part I: The land dynamics (LaD) model. *J. Hydrometeorology*, **3**(3), 283–299.
- Oleson, K. W. and coauthors, 2004: Technical Description of the Community Land Model (CLM). NCAR/TN-464+STR, NCAR TECHNICAL NOTE.
- Prentice, I. C. and coauthors, 2001: The carbon cycle and atmospheric carbon dioxide. *Climate Change 2001: The Scientific Basis*. L. Pitelka and A. Ramirez Rojas, Eds., Cambridge University Press, 183–237.
- Randall, D. A. and coauthors, 1994: Analysis of snow feedbacks in 14 general circulation models. *J. Geophys. Res.*, **99**(D10), 20757–20772.
- Rossow, W. B. and L. C. Garder, 1993a: Cloud detection using satellite measurements of infrared and visible radiances for ISCCP. *J. Climate*, **6**, 2341–2369.
- Rossow, W. B. and L. C. Garder, 1993b: Validation of ISCCP cloud detections. *J. Climate*, **6**, 2370–2393.

- Rossow, W. B. and R. A. Schiffer, 1991: ISCCP cloud data products. *Bull. Amer. Meteor. Soc.*, **72**(1), 2–20.
- Rossow, W. B. and R. A. Schiffer, 1999: Advances in understanding clouds from ISCCP. *Bull. Amer. Meteor. Soc.*, **80**(11), 2261–2287.
- Rossow, W. B., A. W. Walker, D. Beuschel and M. Roiter, 1996: International Satellite Cloud Climatological Project (ISCCP) description of new cloud datasets. WMO/TD 737, World Climate Research Programme (ICSU AND WMO).
- Rossow, W. B., A. W. Walker and L. C. Garder, 1993: Comparison of ISCCP and other cloud amounts. *J. Climate*, **6**, 2394–2418.
- Smith, R. and P. Gent, 2004: Reference Manual for the Parallel Ocean Program POP: Ocean System Model CCSM2.0 AND 3.0. LAUR-02-2484.
- Zhang, Y.-C., W. B. Rossow, A. A. Lacis, V. Oinas and M. M. Mishchenko, 2004: Calculation of radiative fluxes from the surface to top of atmosphere based on ISCCP and other global datasets: Refinements of the radiative transfer model and the input data. *J. Geophys. Res.*, **109**(D19105), 1–27.

Figure captions:

Figure 1: The geographical distribution of changes in climatological springtime-mean surface albedo (α_s), cloud cover (c), logarithm of cloud optical thickness ($\ln(\tau + 1)$) and planetary albedo (α_p) from the climate of the 20th century (1901-2000) to the climate of the 22nd century (2100-2199) in CM2.0 and CCSM3.0 scenario runs. Here, the changes in surface albedo, cloud cover and planetary albedo are all evaluated by percentage points, rather than a fractional change. Surface albedo, cloud cover and planetary albedo are in the units of %, while logarithm of cloud optical thickness is in units of tenths. The same units for each variable are also used in Fig 2.

Figure 2: Changes in climatological springtime-mean surface albedo (α_s), cloud cover (c), logarithm of cloud optical thickness ($\ln(\tau + 1)$) and planetary albedo (α_p) averaged over extratropical North America and Eurasia from the climate of the 20th century (1901-2000) to the climate of the 22nd century (2100-2199) in CM2.0 and CCSM3.0. In the calculations, changes in the climatological springtime-mean values of c , $\ln(\tau + 1)$ and α_p , as shown in Fig 1, were weighted by climatological incoming solar radiation at the top of atmosphere in the climate of the 20th century, while changes in the climatological springtime-mean values of α_s were weighted by climatological incoming solar radiation at the surface in the climate of the 20th century. These techniques were used in all calculations involving spatial averages of c , $\ln(\tau + 1)$, α_p and α_s in this article. Note that extratropical North America encompasses land area northward of 30°N , including Greenland, and extratropical Eurasia is the Eurasian land area northward of 30°N .

Figure 3: Scatter plots of modeled interannual and geographical variations in springtime-mean planetary albedo based on eq. (10) and interannual and geographical variations

in springtime-mean planetary albedo seen in ISCCP, CM2.0 and CCSM3.0 in extratropical North America and Eurasia for the current climate. The current climate refers to the climate of the 1984-2000 period for ISCCP, and the climate of the 20th century for CM2.0 and CCSM3.0. (These same definitions apply to whole paper.) Here, for clarity, we only show 10% of ISCCP data sets and 1% of the two model data sets on this figure. All sub-samples are randomly chosen. This same plotting method is also used in Fig 4.

Figure 4: Scatter plots of modeled interannual and geographical variations in springtime-mean clear-sky planetary albedo and interannual and geographical variations in springtime-mean clear-sky planetary albedo seen in ISCCP, CM2.0 and CCSM3.0 in extratropical North America and Eurasia for the current climate.

Figure 5: The climatological springtime-mean values of T_a^{cr} , $\varepsilon_2 \cdot c \cdot \ln(\tau + 1)$ and $\partial\alpha_p/\partial\alpha_s$ seen in ISCCP, CM2.0 and CCSM3.0 in extratropical North America and Eurasia in the current climate and the future climate (2100-2199). First, regression calculations are performed to obtain values of T_a^{cr} , ε_1 and ε_2 based on eqs. (5) and (10) (see Sections 4 and 5). Then, climatological springtime-mean values of $\varepsilon_2 \cdot c \cdot \ln(\tau + 1)$ are calculated at all locations within extratropical North America and Eurasia. Finally, these values are averaged over extratropical North America and Eurasia, respectively. Note that $\partial\alpha_p/\partial\alpha_s = T_a^{cr} - \varepsilon_2 \cdot c \cdot \ln(\tau + 1)$.

Figure 6: Values of $\partial\alpha_p/\partial\alpha_s$ in extratropical North America and Eurasia in climate simulations. Procedures similar to those demonstrated in the caption of Fig 5 are performed to get these values. See Table 1 for the names of the models. Values of $\partial\alpha_p/\partial\alpha_s$ are available only for 14 of the 17 models because other 4 models do not

provide all variables required by our analytical model. The solid lines in the figure represent the ISCCP values of $\partial\alpha_p/\partial\alpha_s$.

Figure 7: Values of $\Delta\alpha_s/\Delta T_s$ in extratropical North America and Eurasia in climate simulations. Procedures similar to those demonstrated in the caption of Table 2 are performed to get these values. The units are $\%/^{\circ}\text{C}$.

Table captions:

Table 1: A list of 17 models used in this study and the numbers they correspond to in Figs 6 and 7.

Table 2: First row: The changes in climatological springtime-mean surface albedo (the first column), surface air temperature (the second column) averaged over North America from the climate of the 20th century, 1901-2000 to the climate of the 22nd century, 2100-2199 and the ratio of the former to the latter (the third column) in CM2.0. Second row: As in the first row, except for Eurasia. Third row: As in the first row, except for CCSM3.0 data sets. Fourth row: As in the second row, except for CCSM3.0 data sets. Surface albedo is in units of % and surface air temperature is in units of °C.

Table 3: First row: The climatological springtime-mean values of ε_2 (the first column), $c \cdot \ln(\tau + 1)$ (the second column) in the climate of the 20th century and $c \cdot \ln(\tau + 1)$ (the third column) in the climate of the 22nd century in CM2.0 over extratropical North America. Second row: As in the first row, except for extratropical Eurasia. Third row: As in the first row, except for CCSM3.0 data sets. Fourth row: As in the second row, except for CCSM3.0 data sets. Fifth row: The climatological springtime-mean values of ε_2 (the first column), $c \cdot \ln(\tau + 1)$ (the second column) over extratropical North America seen in ISCCP in the current climate, 1984-2000. Sixth row: As in the fifth row, except for extratropical Eurasia.

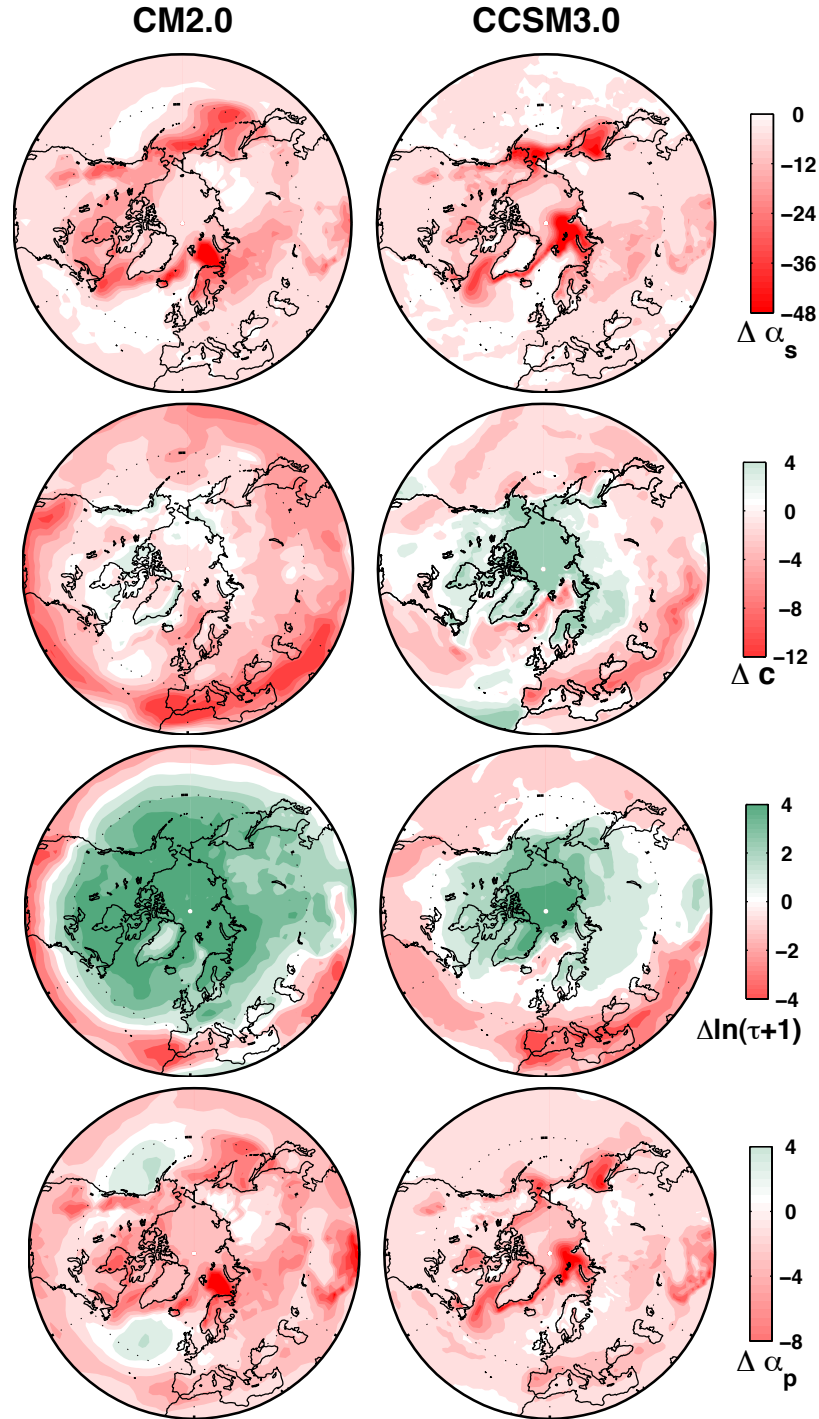


Figure 1: The geographical distribution of changes in climatological springtime-mean surface albedo (α_s), cloud cover (c), logarithm of cloud optical thickness ($\ln(\tau + 1)$) and planetary albedo (α_p) from the climate of the 20th century (1901-2000) to the climate of the 22nd century (2100-2199) in CM2.0 and CCSM3.0 scenario runs. Here, the changes in surface albedo, cloud cover and planetary albedo are all evaluated by percentage points, rather than a fractional change. Surface albedo, cloud cover and planetary albedo are in the units of %, while logarithm of cloud optical thickness is in units of tenths. The same units for each variable are also used in Fig 2.

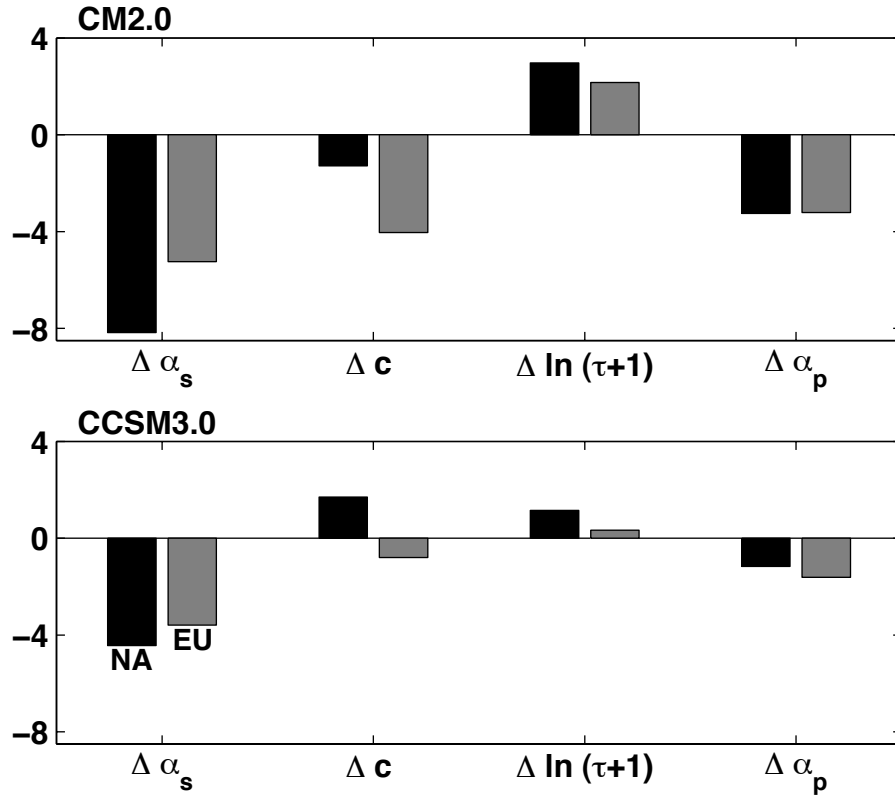


Figure 2: Changes in climatological springtime-mean surface albedo (α_s), cloud cover (c), logarithm of cloud optical thickness ($\ln(\tau + 1)$) and planetary albedo (α_p) averaged over extratropical North America and Eurasia from the climate of the 20th century (1901-2000) to the climate of the 22nd century (2100-2199) in CM2.0 and CCSM3.0. In the calculations, changes in the climatological springtime-mean values of c , $\ln(\tau + 1)$ and α_p , as shown in Fig 1, were weighted by climatological incoming solar radiation at the top of atmosphere in the climate of the 20th century, while changes in the climatological springtime-mean values of α_s were weighted by climatological incoming solar radiation at the surface in the climate of the 20th century. These techniques were used in all calculations involving spatial averages of c , $\ln(\tau + 1)$, α_p and α_s in this article. Note that extratropical North America encompasses land area northward of 30°N , including Greenland, and extratropical Eurasia is the Eurasian land area northward of 30°N .

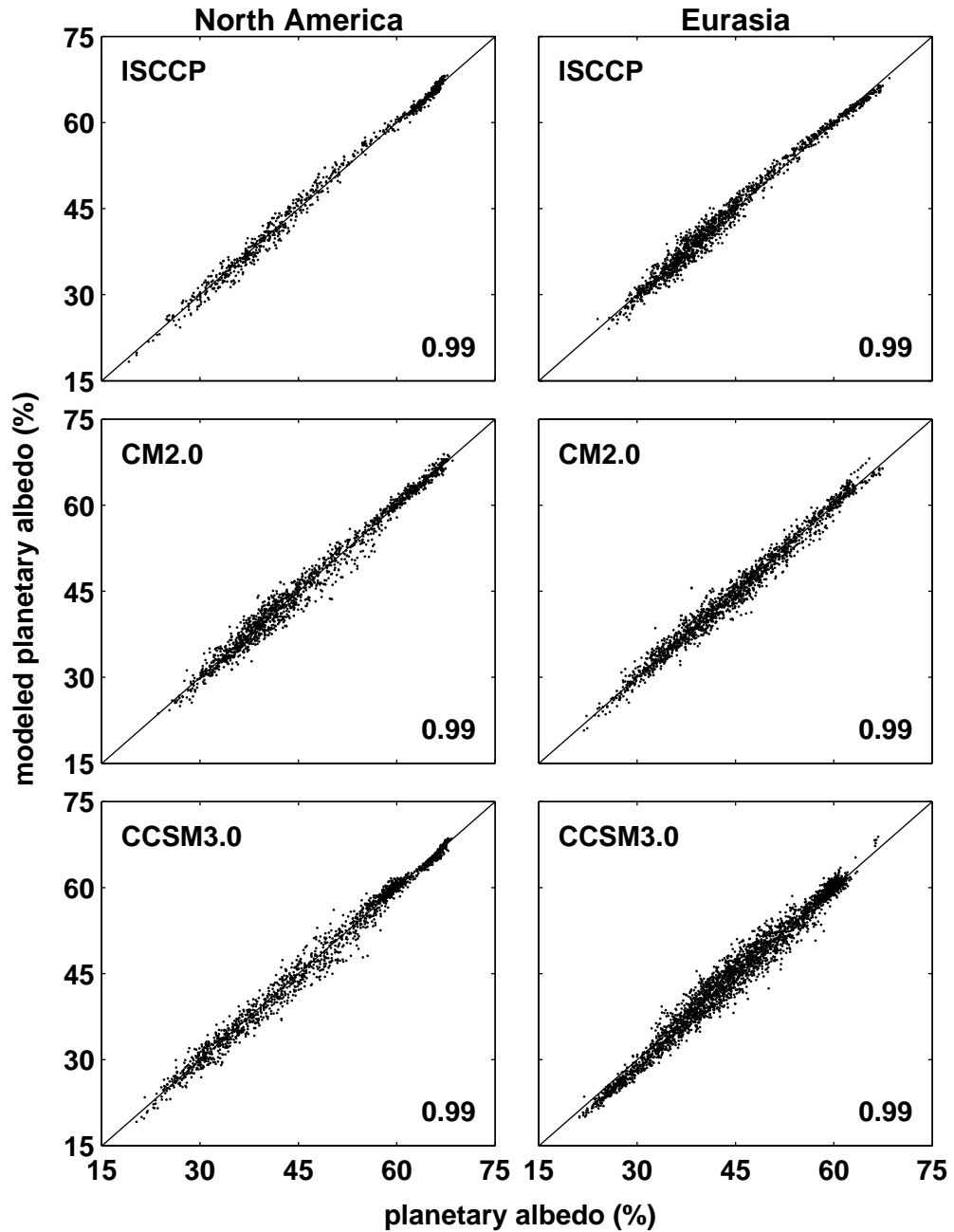


Figure 3: Scatter plots of modeled interannual and geographical variations in springtime-mean planetary albedo based on eq. (10) and interannual and geographical variations in springtime-mean planetary albedo seen in ISCCP, CM2.0 and CCSM3.0 in extratropical North America and Eurasia for the current climate. The current climate refers to the climate of the 1984-2000 period for ISCCP, and the climate of the 20th century for CM2.0 and CCSM3.0. (These same definitions apply to whole paper.) Here, for clarity, we only show 10% of ISCCP data sets and 1% of the two model data sets on this figure. All sub-samples are randomly chosen. This same plotting method is also used in Fig 4.

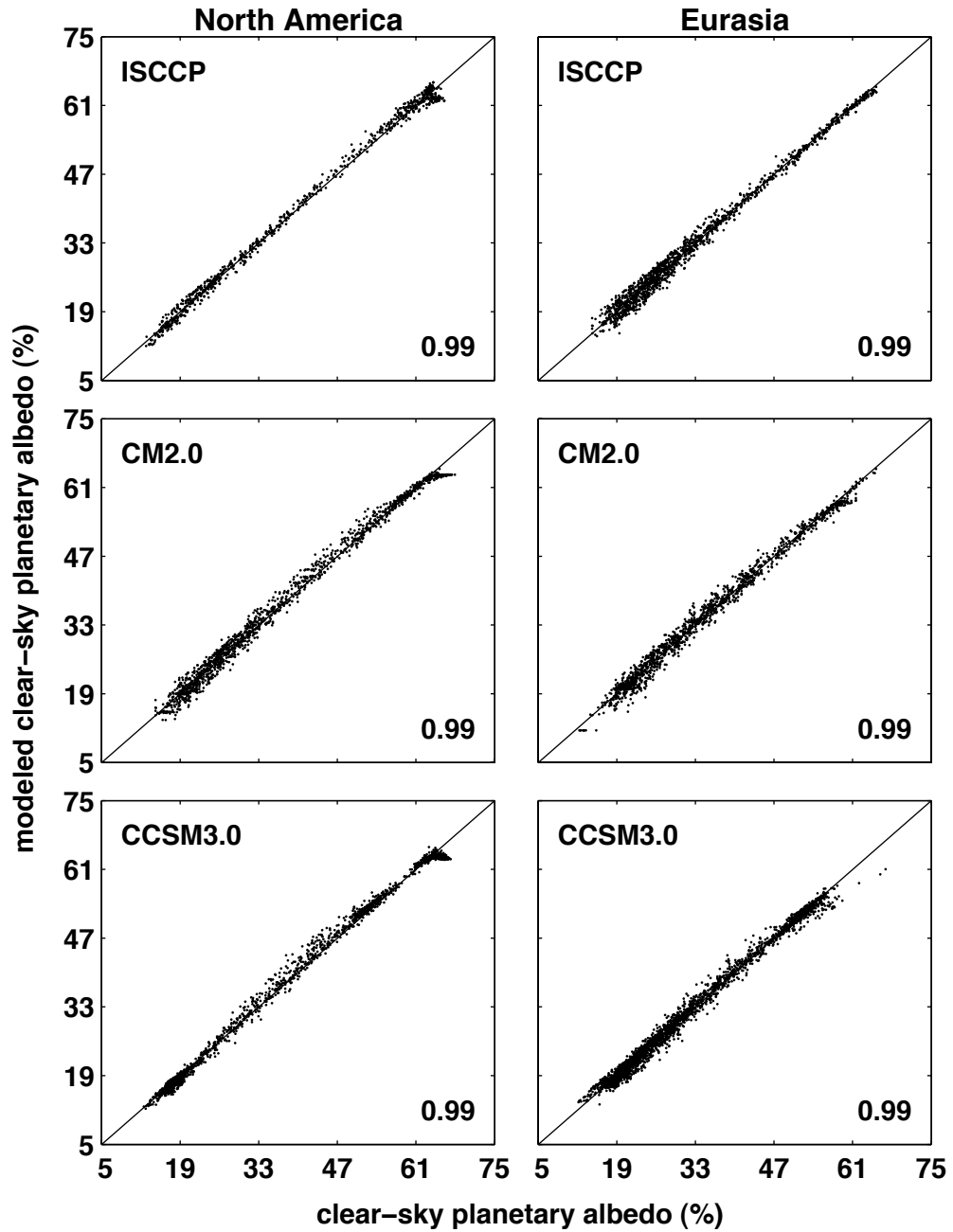


Figure 4: Scatter plots of modeled interannual and geographical variations in springtime-mean clear-sky planetary albedo and interannual and geographical variations in springtime-mean clear-sky planetary albedo seen in ISCCP, CM2.0 and CCSM3.0 in extratropical North America and Eurasia for the current climate.

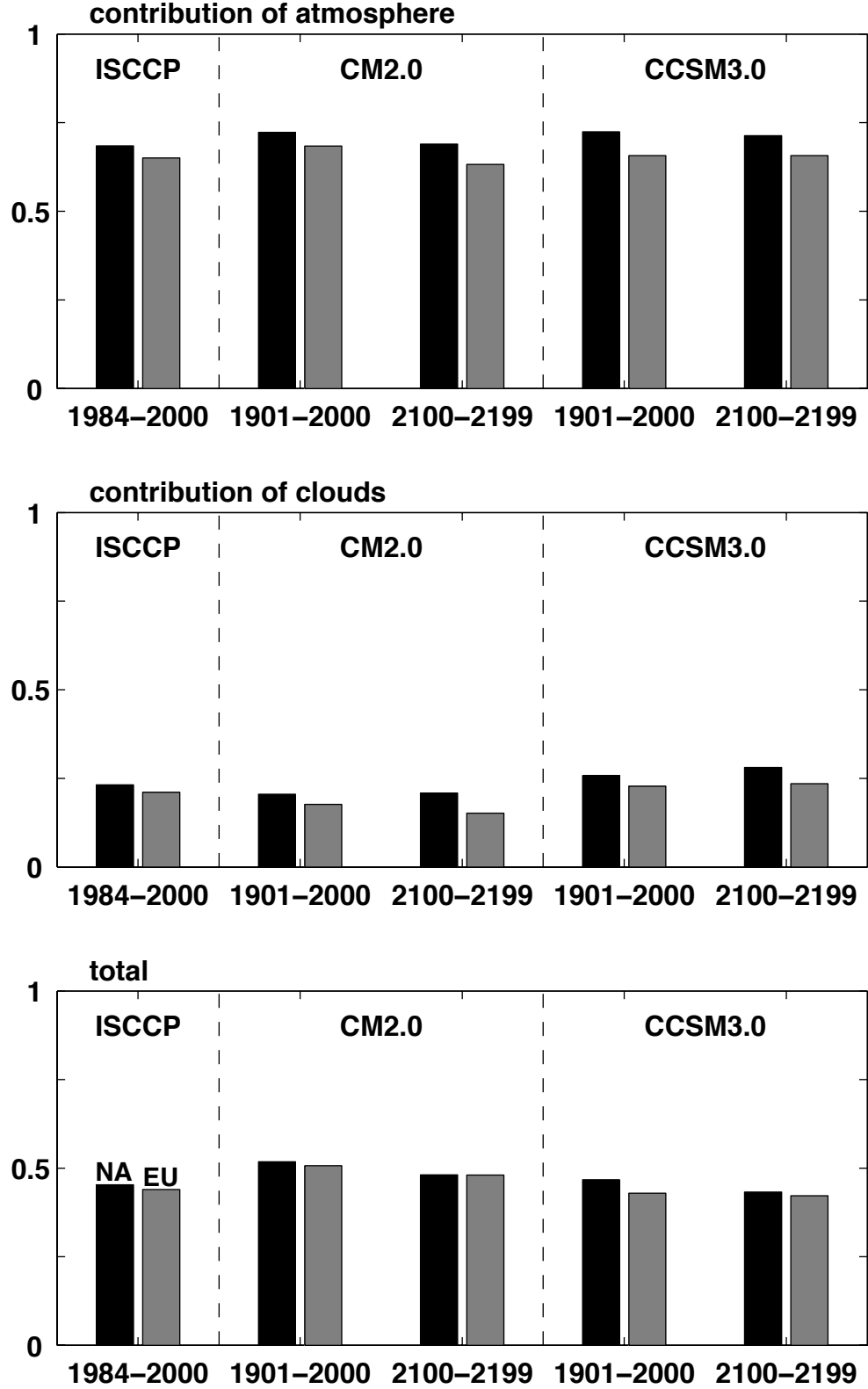


Figure 5: The climatological springtime-mean values of T_a^{cr} , $\varepsilon_2 \cdot c \cdot \ln(\tau + 1)$ and $\partial\alpha_p/\partial\alpha_s$ seen in ISCCP, CM2.0 and CCSM3.0 in extratropical North America and Eurasia in the current climate and the future climate (2100-2199). First, regression calculations are performed to obtain values of T_a^{cr} , ε_1 and ε_2 based on eqs. (5) and (10) (see Sections 4 and 5). Then, climatological springtime-mean values of $\varepsilon_2 \cdot c \cdot \ln(\tau + 1)$ are calculated at all locations within extratropical North America and Eurasia. Finally, these values are averaged over extratropical North America and Eurasia, respectively. Note that $\partial\alpha_p/\partial\alpha_s = T_a^{cr} - \varepsilon_2 \cdot c \cdot \ln(\tau + 1)$.

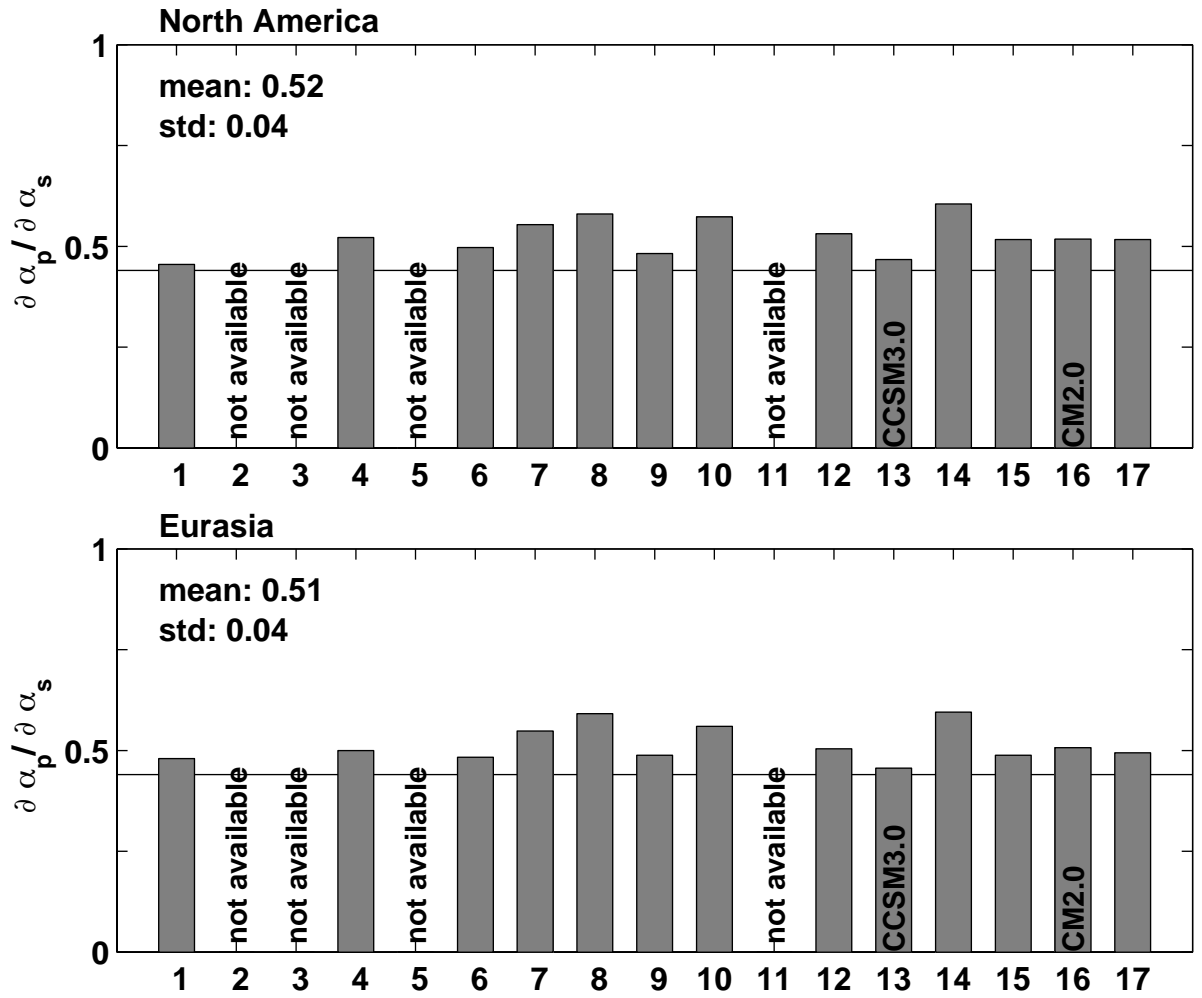


Figure 6: Values of $\partial \alpha_p / \partial \alpha_s$ in extratropical North America and Eurasia in climate simulations. Procedures similar to those demonstrated in the caption of Fig 5 are performed to get these values. See Table 1 for the names of the models. Values of $\partial \alpha_p / \partial \alpha_s$ are available only for 14 of the 17 models because other 4 models do not provide all variables required by our analytical model. The solid lines in the figure represent the ISCCP values of $\partial \alpha_p / \partial \alpha_s$.

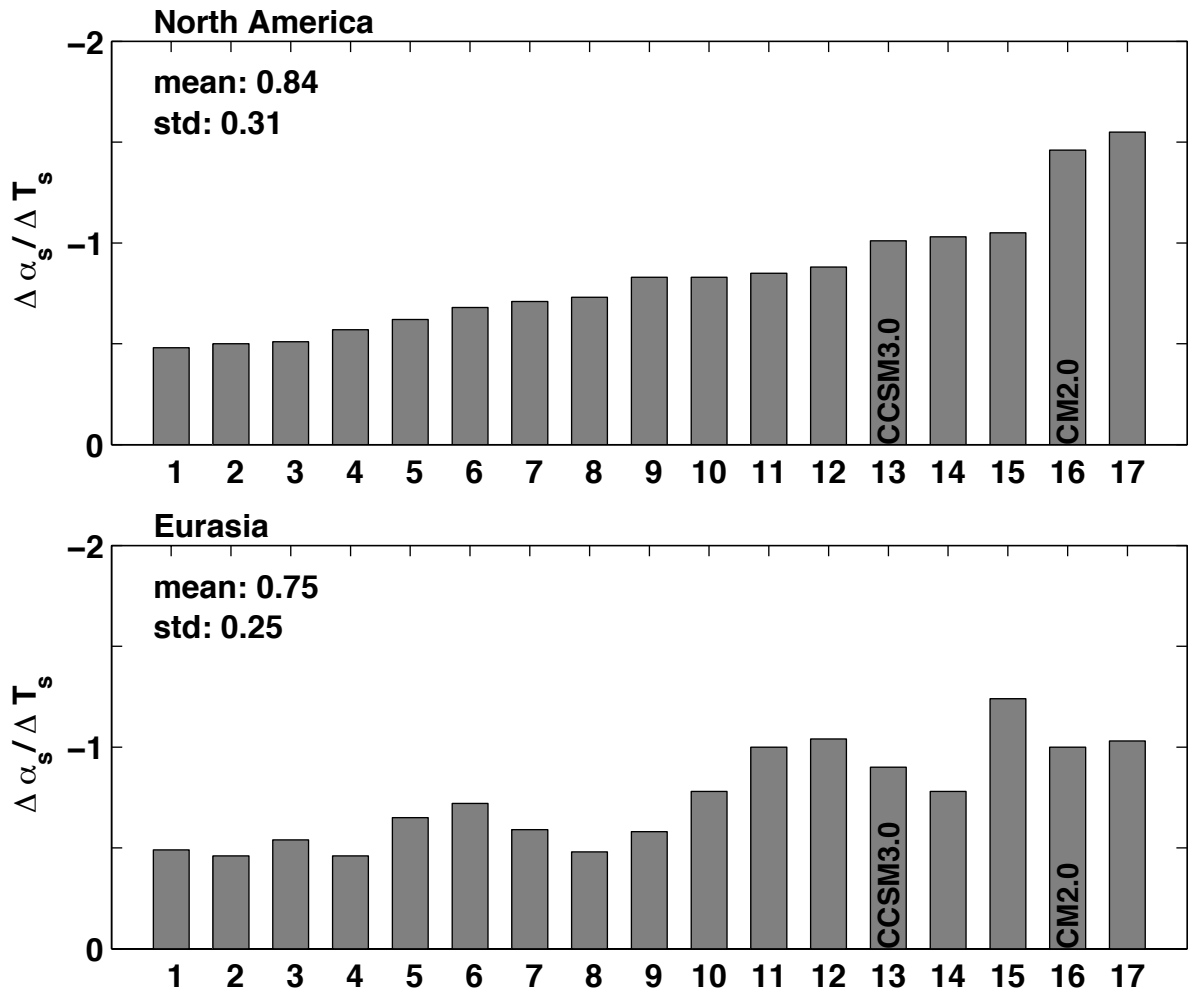


Figure 7: Values of $\Delta\alpha_s/\Delta T_s$ in extratropical North America and Eurasia in climate simulations. Procedures similar to those demonstrated in the caption of Table 2 are performed to get these values. The units are $\%/^{\circ}\text{C}$.

Number	Model
1	cnrm_cm3
2	mri_cgcm2_3_2a
3	giss_model_e_r
4	csiro_mk3_0
5	ncar_pcm1
6	ukmo_hadcm3
7	cccma_cgcm3_1
8	iap_fgoals1_0_g
9	mpi_echam5
10	ukmo_hadgem1
11	miub_echo_g
12	ipsl_cm4
13	ncar_ccsm3.0
14	miroc3_2_medres
15	inmcm3.0
16	gfdl_cm2_0
17	gfdl_cm2_1

Table 1: A list of 17 models used in this study and the numbers they correspond to in Figs 6 and 7.

	Regions	$\Delta\alpha_s$	ΔT_s	$\Delta\alpha_s/\Delta T_s$
CM2.0	N. A.	-8.17	5.58	-1.46
	Eurasia	-5.24	5.26	-1.00
CCSM3.0	N. A.	-4.44	4.40	-1.01
	Eurasia	-3.59	3.97	-0.90

Table 2: First row: The changes in climatological springtime-mean surface albedo (the first column), surface air temperature (the second column) averaged over North America from the climate of the 20th century, 1901-2000 to the climate of the 22nd century, 2100-2199 and the ratio of the former to the latter (the third column) in CM2.0. Second row: As in the first row, except for Eurasia. Third row: As in the first row, except for CCSM3.0 data sets. Fourth row: As in the second row, except for CCSM3.0 data sets. Surface albedo is in units of % and surface air temperature is in units of °C.

	Regions	ε_2	$c \cdot \ln(\tau + 1)$ (1901-2000)	$c \cdot \ln(\tau + 1)$ (2100-2199)
CM2.0	N. A.	0.10	1.95	2.16
	Eurasia	0.10	1.77	1.84
CCSM3.0	N. A.	0.16	1.65	1.77
	Eurasia	0.16	1.40	1.54
ISCCP	N. A.	0.14	1.51	—
	Eurasia	0.14	1.35	—

Table 3: First row: The climatological springtime-mean values of ε_2 (the first column), $c \cdot \ln(\tau + 1)$ (the second column) in the climate of the 20th century and $c \cdot \ln(\tau + 1)$ (the third column) in the climate of the 22nd century in CM2.0 over extratropical North America. Second row: As in the first row, except for extratropical Eurasia. Third row: As in the first row, except for CCSM3.0 data sets. Fourth row: As in the second row, except for CCSM3.0 data sets. Fifth row: The climatological springtime-mean values of ε_2 (the first column), $c \cdot \ln(\tau + 1)$ (the second column) over extratropical North America seen in ISCCP in the current climate, 1984-2000. Sixth row: As in the fifth row, except for extratropical Eurasia.